

# Drying-Mediated Self-Assembled Growth of Transition Metal Dichalcogenide Wires and their Heterostructures

Seoung-Ki Lee, Jae-Bok Lee, Jyoti Singh, Kuldeep Rana, and Jong-Hyun Ahn\*

A substantial amount of research has been performed on 2D materials with the purpose of developing new types of electronic and optoelectronic devices that are unachievable with existing materials.<sup>[1–6]</sup> In particular, transition metal dichalcogenides (TMDs), with the general formula  $\text{MX}_2$ , have received significant attention due to their promising optical and mechanical properties, as well as their electrical characteristics originating from their atomically thin dimensions and finite band gaps.

Many studies on TMDs have been performed based on materials derived from mechanically exfoliated flakes and their subsequent transfer to useful substrates, such as  $\text{SiO}_2$  and sapphire.<sup>[7–9]</sup> However, this approach does not provide the scalability and proper interface required for mass-produced electronic systems and heterostructured devices. Several synthetic approaches have been explored for the preparation of large scale TMD films.<sup>[10–14]</sup> For example, chemical vapor deposition (CVD), which is currently the most successful approach for the synthesis of high quality TMDs, enables the growth of large scale and uniform films with well-controlled numbers of layers.<sup>[12,15]</sup> Moreover, the CVD method can be used to conveniently prepare lateral or vertical heterostructures by alternation of the vapor-phase reactants during growth. In this way, the syntheses of heterojunctions, such as  $\text{MoS}_2$ – $\text{MoSe}_2$ ,  $\text{WS}_2$ – $\text{WSe}_2$ , and  $\text{MoS}_2$ – $\text{WS}_2$  were successfully demonstrated.<sup>[16,17]</sup> Although the CVD can assure good crystallinity and uniformity, the complex and sensitive synthetic conditions and the difficulty associated with the pattern formation required in integrated devices represents a serious limitation. Therefore, a solution-based method is highly desirable as this process would be relatively simple, and the material dimensions and morphologies could be modulated by altering various synthetic parameters.<sup>[14]</sup>

Here, we report an approach toward the tunable growth of TMDs that combines a dip coating process and self-assembly, providing good control of the structural parameters of the synthesized TMDs, i.e., the thickness, shape, and interwire spacing, by adjusting certain parameters, including the internal flow, humidity, and pH of the solution. In addition, we demonstrate that these wire arrays can be conveniently processed to generate heterostructured  $\text{WS}_2/\text{MoS}_2$  wires as well as flexible, transparent devices in combination with graphene electrodes.

Dr. S.-K. Lee, J.-B. Lee, Dr. J. Singh, Dr. K. Rana,  
Prof. J.-H. Ahn  
School of Electrical and Electronic Engineering  
Yonsei University  
50 Yonsei-ro, Seodaemun-Gu, Seoul 120-749, South Korea  
E-mail: ahnj@yonsei.ac.kr



DOI: 10.1002/adma.201501475

Figure 1a depicts the dip coating process for the production of certain classes of TMD structures. First, a piece of  $\text{SiO}_2/\text{Si}$  or quartz wafer is immersed into an aqueous  $(\text{NH}_4)_2\text{MoS}_4$  (or  $(\text{NH}_4)_2\text{WS}_4$ ) solution (0.23% w/v ( $\text{g mL}^{-1}$ ) in DI water) and removed at different speeds to control the drying velocity. As the water evaporates, small nuclei are formed at the solution–substrate interface, and these nuclei initiate the growth of various solid  $(\text{NH}_4)_2\text{MoS}_4$ , or  $(\text{NH}_4)_2\text{WS}_4$  morphologies as intermediate states of  $\text{MoS}_2$  and  $\text{WS}_2$ . The self-assembled TMD morphologies are strongly dependent on the evaporation rate of the solvent and the diffusion rate of the TMD-precursors in solution. Figure 1b,c presents optical images of the self-assembled  $(\text{NH}_4)_2\text{MoS}_4$  structures formed at different evaporation speeds and pH conditions. At very fast evaporation speeds (approximately  $320 \text{ nl s}^{-1}$ ) induced by high temperature ( $80 \text{ }^\circ\text{C}$ ), a uniform thin film of  $(\text{NH}_4)_2\text{MoS}_4$  was formed after the complete removal of the solvent (condition A, Figure 1b) because there was insufficient time to induce the formation of nucleation seeds. In contrast, at evaporation speeds that were two orders of magnitude slower ( $0.67$ – $1.72 \text{ nl s}^{-1}$ ), dendritic structures were formed (condition B, Figure 1c). The dendrite structures have many worm-like stems with a large number small side branches; self-assemblies of these seeds randomly formed on the substrate.

In addition to these two nonoriented phases, the spontaneous formation of well-oriented wire patterns was observed when the acidity of solution increased from pH 6.41 to pH 5.02 at the same evaporation speed as condition B (condition C, Figure 1d). Interestingly, these long wires, which grew from seeds formed in parallel arrays at the initial solution/substrate/air contact line, displayed uniform spacing between the wires without serious distortion of the arrays. The formation of aligned wires can be explained by the “fingering instability” phenomenon.<sup>[18,19]</sup> When the solvent begins evaporating at the solution/substrate contact line, fingering instability induced by the regulation of the evaporation speed, which affects the internal flow of the solution, leads to the periodic formation of nucleation-seed arrays. In turn, this results in the spontaneous growth of regular, unidirectional wire arrays from the seeds during the drying process (Figure 1d). The critical dependence of the directional growth mechanism on the pH variation is not yet clear. However, we believe that the acidity of the reaction media can effectively suppress the gradation of the precursor diffusion, which is the driving force in the generation of the dendrite side-arms and the lateral expansion of the self-assembly, thereby preserving the main stream and, as a result, enhancing the formation of aligned wire arrays.<sup>[20]</sup>

Thus, the evaporation speed, solution concentration and pH are the key factors that control the nucleation and growth processes, which lead to different self-assembled structures.

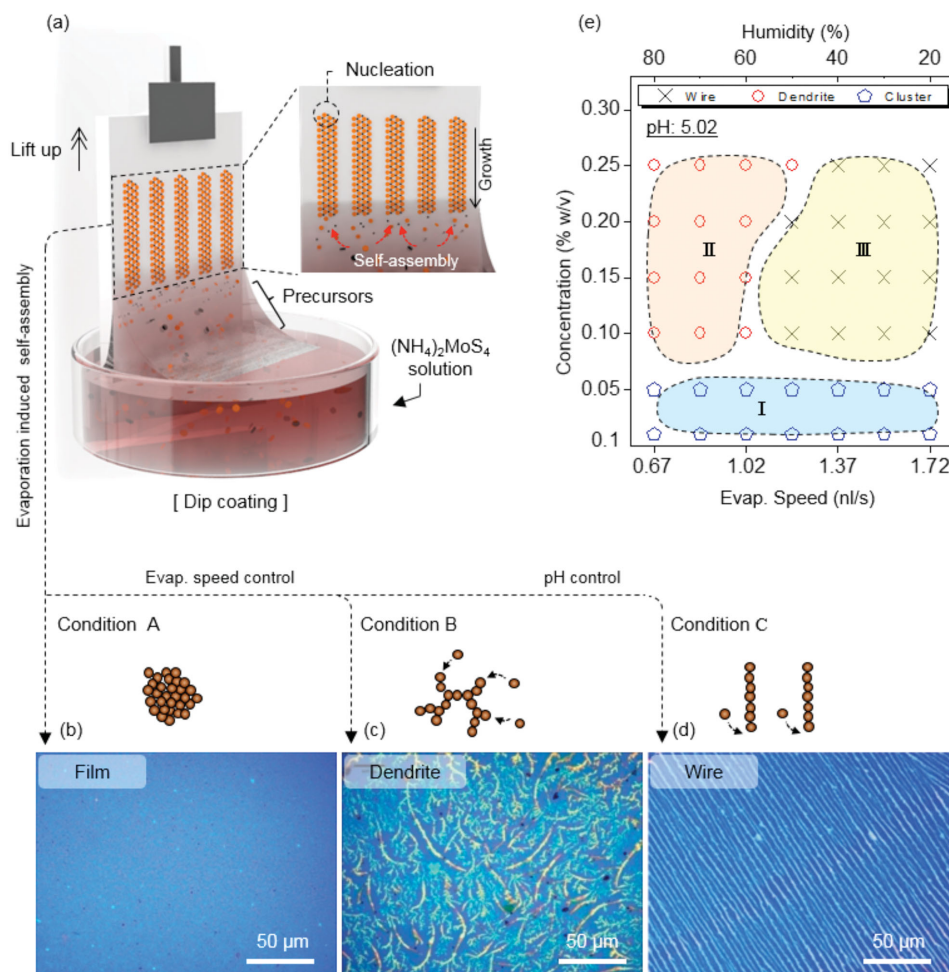


**Figure 1.** Preparation of the self-assembled  $\text{MoS}_2$  structures. a) Schematic illustration of the modified solution process for self-assembled  $\text{MoS}_2$  structures. b–d) Optical images of three different types of self-assembled  $\text{MoS}_2$  structures formed by controlling the evaporation speed of the solution and the solution pH. e) Phase diagram of the self-assembled  $\text{MoS}_2$  structures as a function of the evaporation speed, humidity, and solution concentration.

To investigate the effects of these parameters on the growth of  $\text{MoS}_2$  structures in more detail, the evaporation speed, relative humidity and solution concentration were varied at fixed pH, and the resulting morphologies were examined after full evaporation. Figure 1e shows the phase diagram of  $\text{MoS}_2$  as a function of the three varied factors at fixed acidity, focusing on a window of slow evaporation speeds ranging from 0.67 to 1.72  $\text{nl s}^{-1}$ . When the solution concentration was less than approximately 0.1% w/v (critical concentration), clusters composed of small aggregated particles formed across the entire region, regardless of the evaporation speed and humidity (region I, and Figure S1, Supporting Information). In contrast, at concentrations above this critical concentration, the  $\text{MoS}_2$  morphologies were divided into two distinct regions based on drying speed. These are dendrite (low speed, region II) and wire (high speed, region III). The increase in evaporation speed above approximately 1.2  $\text{nl s}^{-1}$  effectively enhances the segregation of the more concentrated precursor domains, resulting in periodic spacing between nuclei due to the fingering instability, which is similar to the effect observed with increases in the acidity. It is notable that this dry mediate self-assembly is

applicable to other TMDC such as  $\text{WS}_2$  (see the Experimental Section and Figure S2, Supporting Information).

Figure 2a shows captured images of the sequential changes observed as the solvent evaporates (Video S1, Supporting Information). Highly oriented  $(\text{NH}_4)_2\text{MoS}_4$  wires are self-assembled with regular spacing at a velocity of approximately  $15 \mu\text{m s}^{-1}$ . After thermal decomposition, which converts the intermediate materials into  $\text{MoS}_2$ , the change in shape was measured using atomic force microscopy (AFM) (Figure 2b). The average thickness of wires after drying was approximately 90 nm, which was reduced by nearly 62% after thermal annealing, while the width of the wire increased by 10% (from 1.05 to 1.16  $\mu\text{m}$ ) due to out-gassing and an increase in crystallinity. Thermal annealing also changed the arch-shaped surface to a much more smooth and flat surface (rms: 3.12 nm).

The scanning electron microscope (SEM) image of a  $\text{MoS}_2$  wire indicates that the wire maintains continuity without any disconnections or separations despite the geometrical deformation, resulting in an average length of 600–700  $\mu\text{m}$  (Figure 2c,d). However, further increases in length of a few mm are expected if the synthesis and environmental conditions are

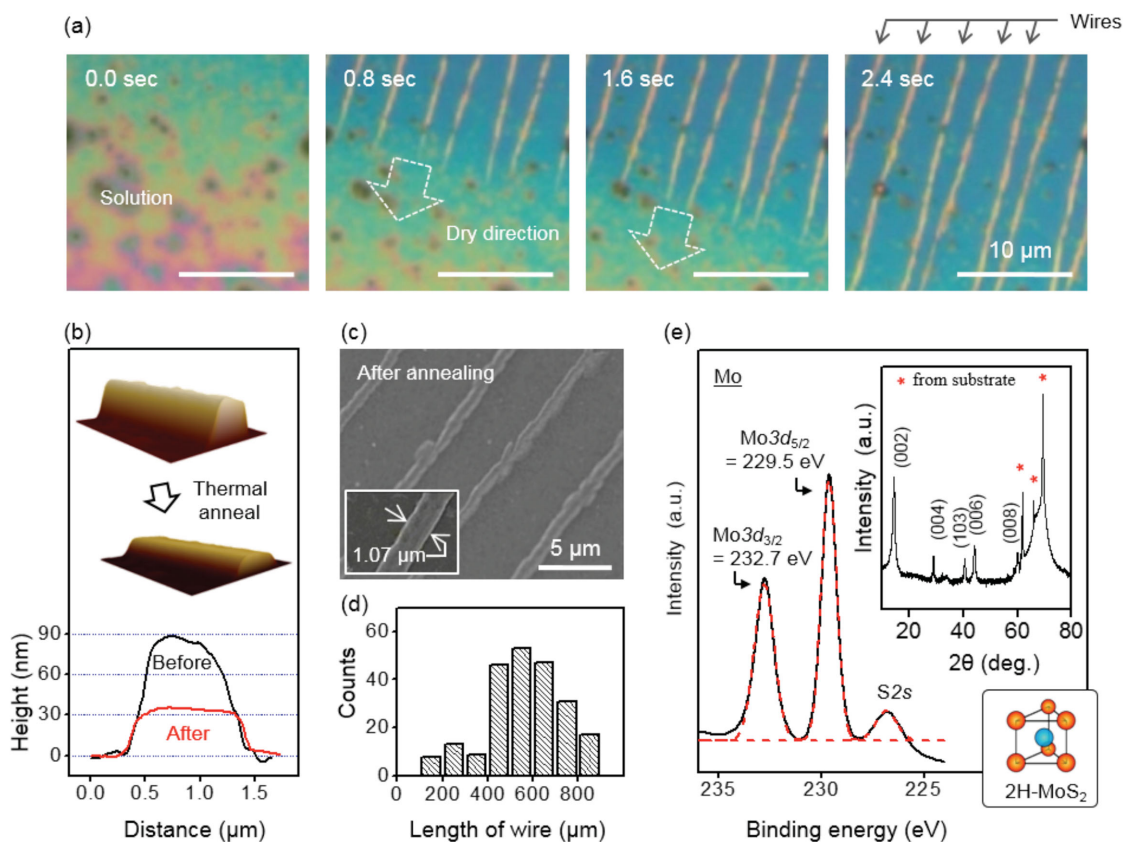


**Figure 2.** Characterization of the self-assembled MoS<sub>2</sub> wires. a) In situ observation of the self-assembled MoS<sub>2</sub> wires. b) Morphology change of the MoS<sub>2</sub> wire before and after thermolysis. c) SEM image of a well-aligned MoS<sub>2</sub> wire array after thermolysis. d) Length distribution of the aligned MoS<sub>2</sub> wires in the unit area. e) XPS spectra of the Mo 3d core level peaks for the MoS<sub>2</sub> wires. Inset: XRD pattern of the MoS<sub>2</sub> wires formed on a SiO<sub>2</sub>/Si substrate.

well-controlled. X-ray photoelectron spectroscopy (XPS) showed the clear characteristics of MoS<sub>2</sub> in the prepared wires (Figure 2e and Figure S3, Supporting Information). Two peaks corresponding to Mo 3d<sub>5/2</sub> and Mo 3d<sub>3/2</sub> were observed at 229.7 and 233.7 eV, respectively. The S 2p exhibited S 2p<sub>3/2</sub> and S 2p<sub>1/2</sub> peaks at 162.9 and 163.9 eV, respectively, which indicated the formation of trigonal prismatic phase (2H-MoS<sub>2</sub>).<sup>[11]</sup> Moreover, X-ray diffraction (XRD) confirmed a high degree of crystallinity in the synthesized MoS<sub>2</sub> wires, displaying intense peaks corresponding to the (002), (004), (103), and (006) crystal planes.<sup>[14,21]</sup>

One of the most important factors in the synthesis of MoS<sub>2</sub> is control of the material thickness. Although the thickness of the synthesized MoS<sub>2</sub> wires can be somewhat reduced by dilution of the reactant solution in the dip coating process, the addition of isopropyl alcohol (IPA), which has a high vapour pressure ( $P_{\text{IPA}}$ : 33.1 mmHg) in solution, proved to be a very effective method for achieving MoS<sub>2</sub> wires with few layers.<sup>[22]</sup> Cross-sectional transmission electron microscopy (TEM) clearly shows a decrease in the wire thickness with the addition of IPA (Figure 3a). The layers of MoS<sub>2</sub> lie parallel on the substrate with a *d*-spacing of 0.63 nm, in agreement with the multilayer MoS<sub>2</sub> shown in the inset of Figure 3a. The MoS<sub>2</sub> wire has a thickness that is higher than 30 nm in the absence of IPA. However, the value decreases to approximately 11 nm, corresponding to approximately 13 layers, after the addition of 16 ppm of

IPA and further decreases to approximately 3 layers after the addition of 60 ppm; because the addition of a small amount of IPA enhances the internal flow in solution (Figure S4, Supporting Information).<sup>[22–24]</sup> In addition, the increased amount of IPA reduced the interspace between wires, which may result from Marangoni instability due to the change in surface tension of the solution coated on the substrate (Figure 3b). The characteristic wavelength of the Marangoni instability ( $\lambda$ ) described by  $\lambda = 2\pi h/a$  (*h* and *a* are the thickness of the water layer, and the dimensionless periodicity of convection, respectively) corresponds to the interspace between wires.<sup>[25]</sup> The addition of volatile IPA induces a decrease in water volume and accordingly reduces a film thickness (*h*). As a result, a decrease in *h* value can reduce the interspace between wires (Figure S4, Supporting Information).

Control of the position and periodic arrangement of MoS<sub>2</sub> wires on a substrate is of significant interest in device fabrication. The position where a substrate is treated with an oxygen plasma can induce aggregation of precursors due to its hydrophilic character, which may further function as nucleation sites for the subsequent growth of MoS<sub>2</sub> wires (Figure 3c). A SEM image clearly shows the stain pattern caused by aggregation on a growing point and controlled growth of MoS<sub>2</sub> wires after dip coating and drying (Figure S5, Supporting Information). However, if the space between the nucleation sites is wider than 40 μm, wires unintentionally grow inside the spaces.

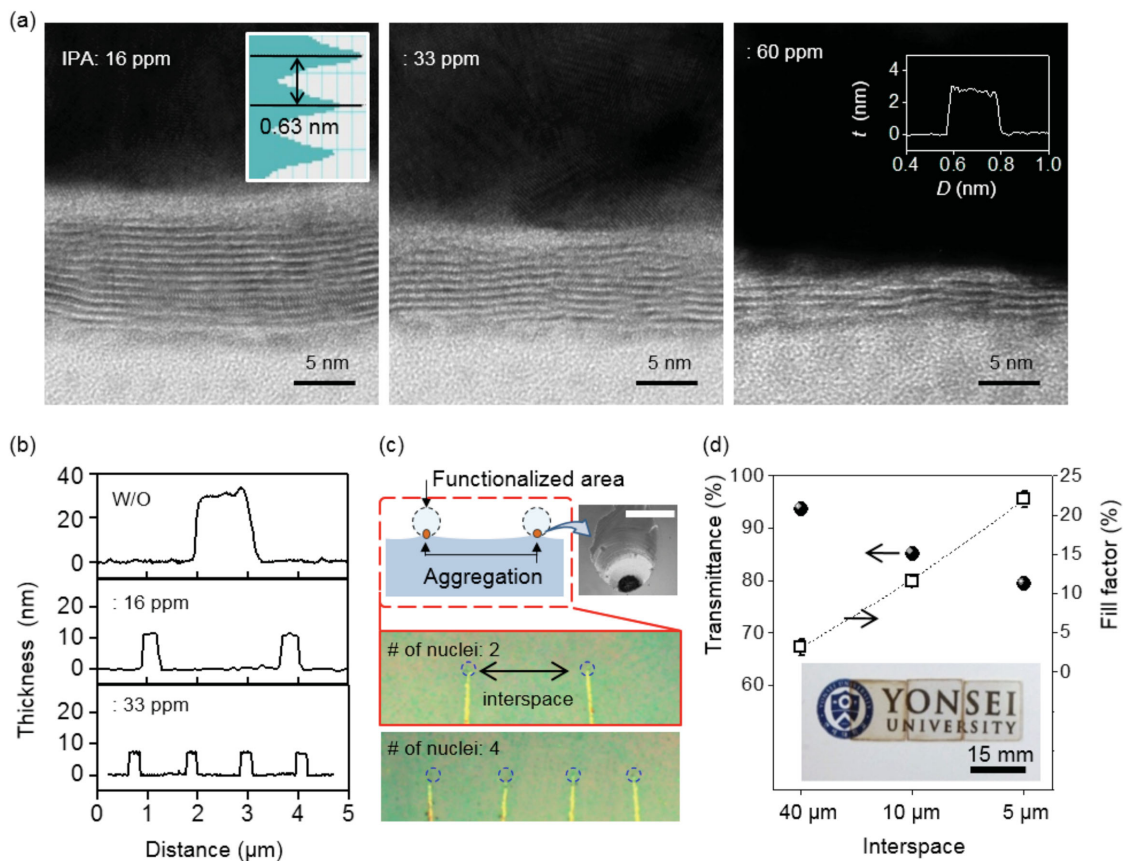


**Figure 3.** Tunable thickness and internal space of self-assembled MoS<sub>2</sub> wires. a,b) The cross-sectional HRTEM images and AFM measurement of the thickness-controlled MoS<sub>2</sub> wires. c) Schematic illustration and optical image of the interspace-controlled MoS<sub>2</sub> wire array (scale bar: 1  $\mu$ m). d) Optical transmittance (at a wavelength of 550 nm) with respect to the wire interspace and corresponding fill factor. Inset: optical image of a MoS<sub>2</sub> wire array on a quartz substrate.

MoS<sub>2</sub> wires can be implemented on other hydrophilic surfaces besides SiO<sub>2</sub>/Si wafer substrates, such as transparent quartz. The inset in Figure 3d shows an optical image of a MoS<sub>2</sub> wire array formed on a quartz substrate with three different wire densities (i.e., 5, 10, and 40  $\mu$ m between wires). The visible text on the layer behind the substrate demonstrates the good optical transmittance of both wires and substrate. The optical transmittance of the wire-substrate system is dependent on the filled area of the MoS<sub>2</sub> wires per unit area (fill factor) on the substrate. Interwire distances of 5, 10, and 40  $\mu$ m correspond to fill factors of 22%, 11%, and 3%, respectively, which result in optical transmissions of approximately 79%, 85%, and 93% at 550 nm, inclusive of the substrate effect, indicating an inverse relationship with the fill factor (Figure 3d). The UV-vis transmission spectrum in the range of 350–800 nm shows the characteristic peaks of MoS<sub>2</sub> at 692 nm (1.79 eV) and 634 nm (1.96 eV), originating in interlayer interactions and spin-orbit splitting (Figure S6, Supporting Information).<sup>[26,27]</sup>

Another important feature of this self-assembled growth method is its processability, allowing for easy formation of TMD heterostructures with controllable lengths, thicknesses, and patterns by continuous growth, which is unachievable by conventional processes. TMD heterostructures could be used for the exploration of a range of fundamental physics and new

device concepts. Our synthetic method is based on control of the radial versus axial growth. First, a MoS<sub>2</sub> wire array with the desired geometry was grown on a substrate as previously described. Then, these MoS<sub>2</sub> wires were dipped into the WS<sub>2</sub> precursor, a (NH<sub>4</sub>)<sub>2</sub>WS<sub>4</sub> solution, to form a WS<sub>2</sub> shell-layer on the MoS<sub>2</sub> wires. In this process, the shell thickness can be controlled by the solution concentration and evaporation speed (Figure 4a and see the Experimental Section). As observed in the optical image of Figure 4b, the self-assembled WS<sub>2</sub> can be classified as one of two types: (1) highly elongated WS<sub>2</sub> covering a MoS<sub>2</sub> wire core or (2) WS<sub>2</sub> wire formed independently on the substrate without MoS<sub>2</sub>. Although WS<sub>2</sub> grows preferentially on MoS<sub>2</sub> wires, which function as a seeding material due to the small lattice mismatch (<1%), WS<sub>2</sub> often forms wires on self-activated nucleation sites.<sup>[28]</sup> Raman single-spectra and mapping images reveal distinct signals from two regions (Figure 4c,d). The pure WS<sub>2</sub> wires on the substrate (marked by A) show signals corresponding to the E<sub>2g</sub> mode at 350 cm<sup>-1</sup> and the A<sub>1g</sub> mode at approximately 418 cm<sup>-1</sup>, confirming the small number of deposited WS<sub>2</sub> layers (Figure 4c).<sup>[28]</sup> WS<sub>2</sub> grown on MoS<sub>2</sub> (marked by B) additionally exhibited two sharp peaks located at 382 and 407 cm<sup>-1</sup>, corresponding to the E<sub>2g</sub> mode and A<sub>1g</sub> mode of MoS<sub>2</sub>. The relative Raman intensities of the E<sub>2g</sub> and A<sub>1g</sub> modes of MoS<sub>2</sub> are maintained without considerable

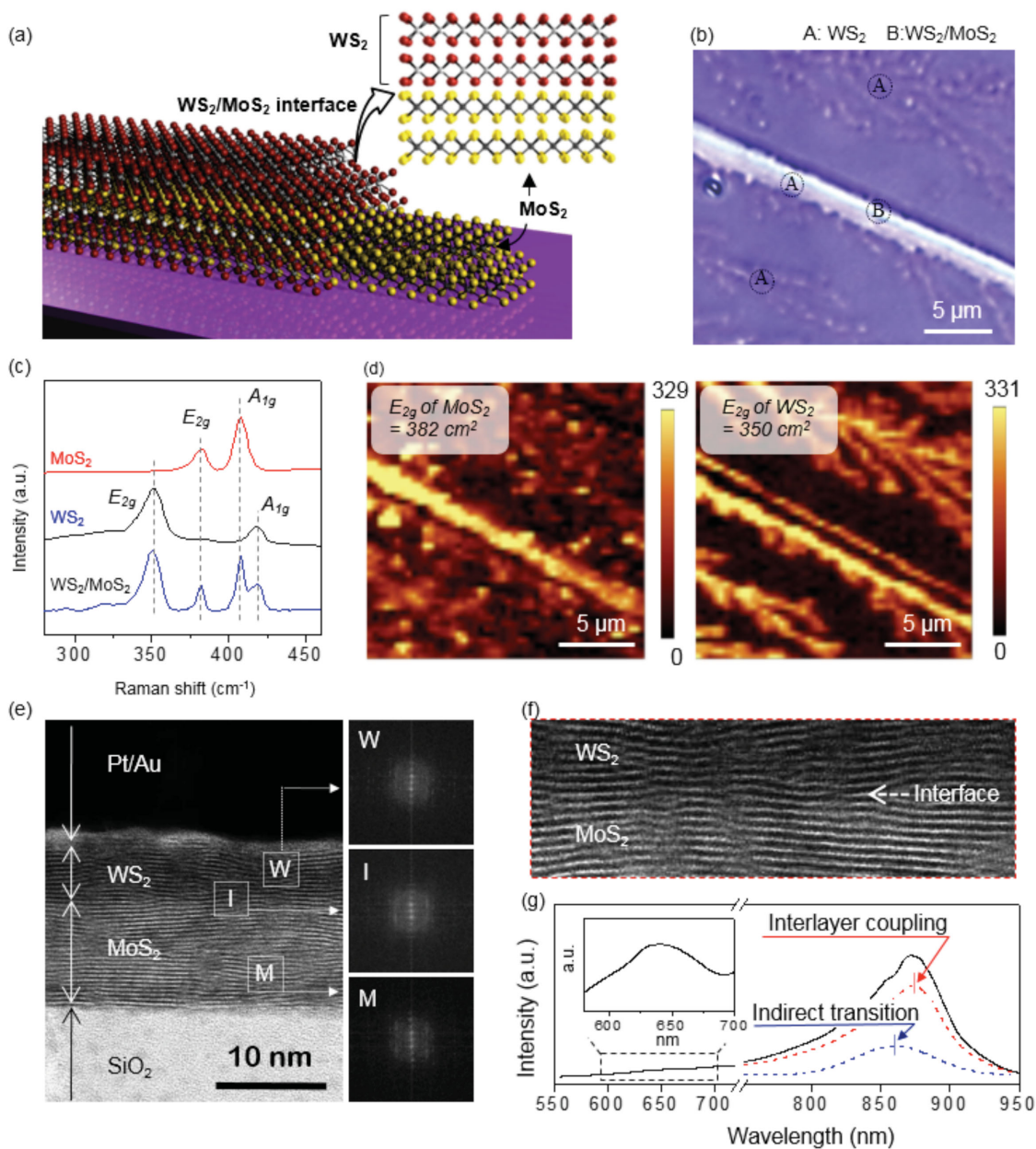


**Figure 4.** Characterization of self-assembled WS<sub>2</sub>/MoS<sub>2</sub> stacked heterostructure. a,b) Schematic illustration and optical image of WS<sub>2</sub>/MoS<sub>2</sub> heterostructure. c) Raman spectra from the areas of MoS<sub>2</sub>, WS<sub>2</sub>, and the WS<sub>2</sub>/MoS<sub>2</sub> heterostructure, which are marked as A and B in (b). d) Raman mapping data taken in the same area as (b). e,f) The cross-sectional HRTEM image of the WS<sub>2</sub>/MoS<sub>2</sub> heterostructure and magnified image of the interfacial area. Right: Fourier transform images from the selected area. g) Typical photoluminescence spectra of a self-assembled WS<sub>2</sub>/MoS<sub>2</sub> heterostructure.

changes before and after WS<sub>2</sub> formation, which involves a long thermal annealing process. We believe that the sulfur-rich WS<sub>2</sub> precursor-shell may shield the MoS<sub>2</sub> core from damage during WS<sub>2</sub> thermolysis.<sup>[14]</sup>

The interface of the WS<sub>2</sub>/MoS<sub>2</sub> heterostructure was identified using TEM (Figure 4e,f). Due to their different atomic numbers, WS<sub>2</sub> shows a higher image contrast than the MoS<sub>2</sub> layer. As shown in the cross sectional HRTEM image, there is no interlayer separation, which often originates from trapped molecules and residual polymers in the fabrication of heterostructures synthesized using conventional methods, such as the

pick-up and transfer or manual integration methods.<sup>[29]</sup> Fast Fourier transform (FFT) images show the well-ordered characteristics of a MoS<sub>2</sub> core, WS<sub>2</sub> shell, and their interface. The PL spectrum of these WS<sub>2</sub>/MoS<sub>2</sub> heterostructures exhibits three emission peaks at 640 nm (1.94 eV), 860 nm (1.44 eV), and 872 nm (1.42 eV). The weak peak at 640 nm can be attributed to the interlayer coupling at the imperfect MoS<sub>2</sub>/WS<sub>2</sub> junction. Tongay et al. recently reported that this emission peak originates from spatial inhomogeneities in the MoS<sub>2</sub>/WS<sub>2</sub> heterostructure due to trapped residues, and hence, cannot appear in heterostructures with perfect interfaces.<sup>[30]</sup> In Figure 4f, the existence

of spatial defects at the interface between MoS<sub>2</sub> and WS<sub>2</sub> is observed, which may lead to the emergence of additional peaks due to junction inhomogeneity in a manner similar to trapped residues. The peak at 860 nm arises from the indirect band excitonic transition from multilayered, bulk WS<sub>2</sub> (Figure S7, Supporting Information).<sup>[31]</sup> For the strong emission peak at 872 nm, we believe that it originates primarily from the phonon-assisted optical transition across the indirect band gap through strong interlayer coupling of heterostructures.<sup>[16,30]</sup>

The spontaneous formation of well-aligned TMD wire arrays offers many attractive opportunities for use in electronic devices with new capabilities. We first evaluated the electrical properties of the synthesized MoS<sub>2</sub> wires through the fabrication of field effect transistors. **Figure 5a** shows the conductivity ( $\sigma = [L/W] \times [I_d/V_d]$ ) versus gate voltage ( $V_g$ ) curve of transistors composed of wires with thicknesses of 5 and 32 nm. The electrolyte was used as a gate dielectric because it generates favourable gating properties through the formation of conformal contacts with the wire surfaces. Interestingly, a transistor composed of a thick MoS<sub>2</sub> wire exhibits symmetric ambipolar

conduction, while one made from thin wire shows unipolar, n-type behavior. The origin of the difference in carrier type is not yet clear, but we assume that the altered internal flow, which was increased by the addition of IPA to the solution to reduce the wire thickness, may create Mo and/or S vacancies inside the MoS<sub>2</sub> wire, which affect the semiconducting properties.<sup>[32]</sup> Another possibilities stem from the substrate and the dielectric layer effects,<sup>[33]</sup> and the unintended inclusion of residues from the organic solvent that can work as n-type donor impurities, even in very small amounts.<sup>[14]</sup> The effective electron mobility ( $\mu_{\text{FET}}$ ) of these devices increases gradually with the thickness of the wire from approximately 7 cm<sup>2</sup> V<sup>-1</sup> s<sup>-1</sup> at 5 nm to a saturated level of approximately 100 cm<sup>2</sup> V<sup>-1</sup> s<sup>-1</sup> at 20 nm thick wires (Figure 5b). This mobility variation according to the thickness can be explained by the carrier scattering and the defects of wire surface. Thin MoS<sub>2</sub> wires are strongly influenced by surface defects and interfacial Coloumb impurities such as dangling bonds and chemical residues. In contrast, thicker wires are less vulnerable to the carrier scattering and consequently exhibit higher mobility.<sup>[33,34]</sup>

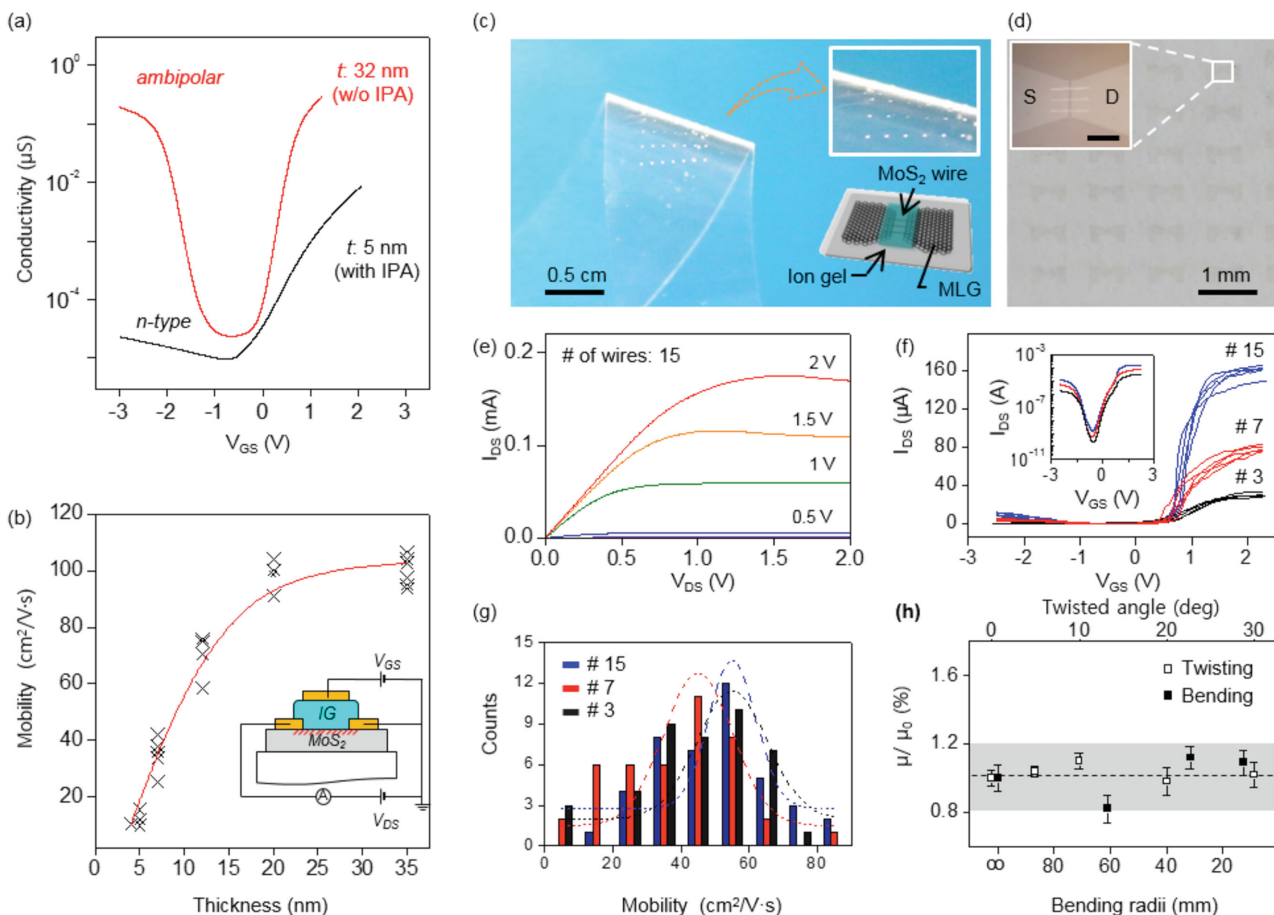


**Figure 5.** Electrical and mechanical characterization of the MoS<sub>2</sub> wire-based device. a) Transfer characteristic of MoS<sub>2</sub>-wire-based transistors with thicknesses of 32 and 5 nm. b) Field effect electron mobility as a function of MoS<sub>2</sub> wire thicknesses. The inset shows a schematic of a top electrolyte gated transistor. c,d) Optical photograph and microscope image of a flexible MoS<sub>2</sub>/graphene hybrid transistor on a transparent plastic substrate. e,f) Output characteristic of a MoS<sub>2</sub>/graphene hybrid transistor ( $V_{\text{DS}}$  vs  $I_{\text{DS}}$ ) and corresponding transfer characteristics ( $V_{\text{GS}}$  vs  $I_{\text{DS}}$ ) with linear and semilogarithmic scales (inset). The number (# symbol) indicates the numbers of wires in the channel. g) A histogram of the field effect mobility of a MoS<sub>2</sub>/graphene hybrid transistor. h) The change in carrier mobility during deformation of the substrate.

An interesting aspect of TMD-based devices is their mechanical bendability and optical transmittance. This characteristic is important for applications in flexible and transparent electronics; these systems might be attractive candidates for these applications due to their enhanced capabilities in these respects compared to conventional oxide-based materials. As a strategy to enable devices with high transmittances and mechanical flexibilities, multilayered graphene was selected as a source/drain electrode (Figure 5c). Moreover, the number of wires between channels can be systematically tuned in the growth step using the previously described method to control the number and position of the nucleation seeds (Figure 5d). Devices with this design have transparencies up to 78% (Figure 5c,d). This degree of transparency compares well with technologies that use inorganic oxides as electronic materials.<sup>[35,36]</sup>

The resulting MoS<sub>2</sub> wire-based transistor exhibited linear current-voltage ( $I_{ds}-V_{ds}$ ) characteristics at small bias, indicating quasi-Ohmic contact with multilayered graphene, which is consistent with previous work.<sup>[37,38]</sup> The transfer characteristics show current enhancement with increasing numbers of wires (3, 7, and 15), indicating that the output current is adjustable by controlling of the number of wires (Figure 5e,f). The average effective mobility ( $\mu_{FET}$ ), evaluated from 42 devices on a single device substrate, was approximately 45 cm<sup>2</sup> V<sup>-1</sup> s<sup>-1</sup>. This result is somewhat lower than the values found for devices composed of conventional metal electrodes, as shown in Figure 5b, due to the contact resistance between the MoS<sub>2</sub> and the graphene (Figure 5g). The on/off current ratio and subthreshold slope were calculated to be approximately 10<sup>4</sup> and 194 mV dec<sup>-1</sup>, respectively. The electrical properties of these transistors are also similar to those of typical oxide-based devices.<sup>[39,40]</sup> For more realistic applications, further characterization was performed to study the mechanical properties of the flexible MoS<sub>2</sub> transistor on PET substrates during bending and twisting with a home-built equipment (Figure S8, Supporting Information). The PET substrate holding the MoS<sub>2</sub> wire-based transistor was bent in the direction vertical to the channel length from flat to a curvature radius of 20 mm (strain of 0.8%). As shown in Figure 5h, the transistor maintained stable operation even under distortion by bending and twisting (maximum twisting angle: 30°). These features make MoS<sub>2</sub> wires attractive for applications requiring high degrees of mechanical bending, such as flexible or conformable electronic systems.

In summary, we demonstrated the synthesis of solution-based self-assembled MoS<sub>2</sub> and WS<sub>2</sub> wire arrays via a modified thermolysis method. The structures, thicknesses, and repetition period of the self-assembled wire arrays were controlled by regulating the internal flow of the precursor solution. As a practical application, WS<sub>2</sub>/MoS<sub>2</sub> heterojunctions with clean and geometrically well-aligned interfaces and a MoS<sub>2</sub> wire-based hybrid transistor with a graphene electrode for improved optical transmittance and mechanical flexibility were successfully built on several substrates, including SiO<sub>2</sub>/Si wafer, quartz, and plastic. This tunable and scalable self-assembly method has potential applications within the field of optical and electrical applications, paving the way to new and innovative TMDC-based heterodevices.

## Supporting Information

Supporting Information is available from the Wiley Online Library and from the author.

## Acknowledgements

This work was supported by the Global Frontier Research Center for Advanced Soft Electronics (2014M3A6A5060933) and the Research Program (2009-0083540) through the National Research Foundation of Korea (NRF), funded by the Ministry of Education, Science and Technology and the Yonsei University Future-leading Research Initiative.

Received: March 28, 2015

Revised: April 30, 2015

Published online: June 2, 2015

- [1] K. Novoselov, D. Jiang, F. Schedin, T. Booth, V. Khotkevich, S. Morozov, A. Geim, *Proc. Natl. Acad. Sci. USA* **2005**, *102*, 10451.
- [2] C. Dean, L. Wang, P. Maher, C. Forsythe, F. Ghahari, Y. Gao, J. Katoch, M. Ishigami, P. Moon, M. Koshino, T. Taniguchi, K. Watanabe, K. L. Shepard, J. Hone, P. Kim, *Nature* **2013**, *497*, 598.
- [3] M. Chhowalla, H. S. Shin, G. Eda, L.-J. Li, K. P. Loh, H. Zhang, *Nat. Chem.* **2013**, *5*, 263.
- [4] A. M. van der Zande, P. Y. Huang, D. A. Chenet, T. C. Berkelbach, Y. You, G.-H. Lee, T. F. Heinz, D. R. Reichman, D. A. Muller, J. C. Hone, *Nat. Mater.* **2013**, *12*, 554.
- [5] A. Splendiani, L. Sun, Y. Zhang, T. Li, J. Kim, C.-Y. Chim, G. Galli, F. Wang, *Nano Lett.* **2010**, *10*, 1271.
- [6] L. Li, Y. Yu, G. J. Ye, Q. Ge, X. Ou, H. Wu, D. Feng, X. H. Chen, Y. Zhang, *Nat. Nanotechnol.* **2014**, *9*, 372.
- [7] B. Radisavljevic, A. Radenovic, J. Brivio, V. Giacometti, A. Kis, *Nat. Nanotechnol.* **2011**, *6*, 147.
- [8] K. F. Mak, C. Lee, J. Hone, J. Shan, T. F. Heinz, *Phys. Rev. Lett.* **2010**, *105*, 136805.
- [9] C. Lee, H. Yan, L. E. Brus, T. F. Heinz, J. Hone, S. Ryu, *ACS Nano* **2010**, *4*, 2695.
- [10] Z. Zeng, Z. Yin, X. Huang, H. Li, Q. He, G. Lu, F. Boey, H. Zhang, *Angew. Chem. Int. Ed.* **2011**, *50*, 11093.
- [11] G. Eda, H. Yamaguchi, D. Voiry, T. Fujita, M. Chen, M. Chhowalla, *Nano Lett.* **2011**, *11*, 5111.
- [12] Y.-H. Lee, L. Yu, H. Wang, W. Fang, X. Ling, Y. Shi, C.-T. Lin, J.-K. Huang, M.-T. Chang, C.-S. Chang, *Nano Lett.* **2013**, *13*, 1852.
- [13] Q. Li, J. Newberg, E. Walter, J. Hemminger, R. Penner, *Nano Lett.* **2004**, *4*, 277.
- [14] K.-K. Liu, W. Zhang, Y.-H. Lee, Y.-C. Lin, M.-T. Chang, C.-Y. Su, C.-S. Chang, H. Li, Y. Shi, H. Zhang, C.-S. Lai, L.-J. Li, *Nano Lett.* **2012**, *12*, 1538.
- [15] Y. Lee, J. Lee, H. Bark, I.-K. Oh, G. H. Ryu, Z. Lee, H. Kim, J. H. Cho, J.-H. Ahn, C. Lee, *Nanoscale* **2014**, *6*, 2821.
- [16] Y. Gong, J. Lin, X. Wang, G. Shi, S. Lei, Z. Lin, X. Zou, G. Ye, R. Vajtai, B. I. Yakobson, H. Terrones, M. Terrones, B. K. Tay, J. Lou, S. T. Pantelides, Z. Liu, W. Zhou, P. M. Ajayan, *Nat. Mater.* **2014**, *13*, 1135.
- [17] X. Duan, C. Wang, J. C. Shaw, R. Cheng, Y. Chen, H. Li, X. Wu, Y. Tang, Q. Zhang, A. Pan, J. Jiang, R. Yu, Y. Huang, X. Duan, *Nat. Nanotechnol.* **2014**, *9*, 1024.
- [18] A. Cazabat, F. Heslot, S. Troian, P. Carles, *Nature* **1990**, *346*, 824.
- [19] S. D. Fitzgerald, A. W. Woods, *Nature* **1994**, *367*, 450.
- [20] S.-K. Chan, H.-H. Reimer, M. Kahlweit, *J. Cryst. Growth* **1976**, *32*, 303.

- [21] M. R. Laskar, L. Ma, S. Kannappan, P. S. Park, S. Krishnamoorthy, D. N. Nath, W. Lu, Y. Wu, S. Rajan, *Appl. Phys. Lett.* **2013**, *102*, 252108.
- [22] M. S. Kim, S. Lee, J. H. Koo, J. Hong, Y. Chung, K. J. Son, W.-G. Koh, T. Lee, *ACS Appl. Mater. Interfaces* **2012**, *4*, 5162.
- [23] Y. Feldman, E. Wasserman, D. Srolovitz, R. Tenne, *Science* **1995**, *267*, 222.
- [24] W. Shyy, R. Narayanan, *Fluid Dynamics at Interfaces*, Cambridge University Press, Cambridge, UK **1999**.
- [25] Y. J. Cai, B.-m. Zhang Newby, *J. Am. Chem. Soc.* **2008**, *130*, 6076.
- [26] R. Coehoorn, C. Haas, R. De Groot, *Phys. Rev. B* **1987**, *35*, 6203.
- [27] L. Liang, V. Meunier, *Nanoscale* **2014**, *6*, 5394.
- [28] A. Berkdemir, H. R. Gutiérrez, A. R. Botello-Méndez, N. Perea-López, A. L. Elías, C.-I. Chia, B. Wang, V. H. Crespi, F. López-Urías, J.-C. Charlier, *Sci. Rep.* **2013**, *3*, 1755.
- [29] J. Tan, A. Avsar, J. Balakrishnan, G. Koon, T. Taychatanapat, E. O'Farrell, K. Watanabe, T. Taniguchi, G. Eda, A. C. Neto, *Appl. Phys. Lett.* **2014**, *104*, 183504.
- [30] S. Tongay, W. Fan, J. Kang, J. Park, U. Koldemir, J. Suh, D. S. Narang, K. Liu, J. Ji, J. Li, *Nano Lett.* **2014**, *14*, 3185.
- [31] W. Zhao, Z. Ghorannevis, L. Chu, M. Toh, C. Kloc, P.-H. Tan, G. Eda, *ACS Nano* **2012**, *7*, 791.
- [32] C. Ataca, S. Ciraci, *J. Phys. Chem. C* **2011**, *115*, 13303.
- [33] W. Bao, X. Cai, D. Kim, K. Sridhara, M. S. Fuhrer, *Appl. Phys. Lett.* **2013**, *102*, 042104.
- [34] S.-L. Li, K. Wakabayashi, Y. Xu, S. Nakaharai, K. Komatsu, W.-W. Li, Y.-F. Lin, A. Aparecido-Ferreira, K. Tsukagoshi, *Nano Lett.* **2013**, *13*, 3546.
- [35] E. N. Dattoli, Q. Wan, W. Guo, Y. Chen, X. Pan, W. Lu, *Nano Lett.* **2007**, *7*, 2463.
- [36] S. Ju, A. Facchetti, Y. Xuan, J. Liu, F. Ishikawa, P. Ye, C. Zhou, T. J. Marks, D. B. Janes, *Nat. Nanotechnol.* **2007**, *2*, 378.
- [37] J. Yoon, W. Park, G. Y. Bae, Y. Kim, H. S. Jang, Y. Hyun, S. K. Lim, Y. H. Kahng, W. K. Hong, B. H. Lee, *Small* **2013**, *9*, 3.
- [38] T. Roy, M. Tosun, J. S. Kang, A. B. Sachid, S. B. Desai, M. Hettick, C. C. Hu, A. Javey, *ACS Nano* **2014**, *8*, 6259.
- [39] M. Esro, G. Vourlias, C. Somerton, W. I. Milne, G. Adamopoulos, *Adv. Funct. Mater.* **2015**, *25*, 134.
- [40] K.-C. Ok, H.-J. Jeong, H.-S. Kim, J.-S. Park, *IEEE Electron Device Lett.* **2015**, *36*, 38.